# A flexible high-precision photoacoustic retinal prosthesis

Audrey Leong[†], Yueming Li[†], Thijs R. Ruikes[†], Julien Voillot, Yuhao Yuan, Guo Chen, Arnaud Facon, Chakrya-Anna Chhuon, Corentin Joffrois, Gilles Tessier, Marion Cornebois, Julie Dégardin, Jean-Damien Louise, Ji-Xin Cheng*, Chen Yang*, Hélène Moulet[#]*, Serge Picaud[#]*.

† equal contributions, # equal contributions

A. Leong, T.R. Ruikes, C. Joffrois, G. Tessier, M. Cornebois, J. Dégardin and S. Picaud*
Sorbonne Université, CNRS, INSERM, Institut de la Vision, F-75012 Paris, France
Email: serge.picaud@inserm.fr

Y. Li, Y. Yuan, G. Chen
Department of Electrical and Computer Engineering,
Boston University,
Boston, MA, 02215, United States

J-X Cheng*
Department of Electrical and Computer Engineering and Department of Biomedical Engineering,
Boston University,
Boston, MA, 02215, United States
Email: jxcheng@bu.edu

C. Yang*
Department of Electrical and Computer Engineering and Department of Chemistry,
Boston University,
Boston, MA, 02215, United States
Email: cheyang@bu.edu

J. Voillot, A. Facon, C-A Chhuon, J-D Louise, H Moulet*
Axorus SAS,
Loos, 59120, France
Email: helene.moulet@axorus.com

## Abstract

Retinal degenerative diseases of photoreceptors are a leading cause of blindness with no effective treatment. Retinal prostheses aim to restore sight by stimulating remaining retinal cells. Here, we present a photoacoustic retinal stimulation technology. We designed a polydimethylsiloxane and carbon-based flexible film that converts near-infrared laser pulses into a localized acoustic field with 56-µm lateral resolution, aiming at high-precision acoustic stimulation of mechanosensitive retinal cells. This photoacoustic stimulation resulted in robust and localized modulation of retinal ganglion cell activity in both wild-type and degenerated *ex vivo* retinae. When a millimeter-sized photoacoustic film was implanted in the rat subretinal space, pulsed laser stimulation generated neural modulation *in vivo* along the visual pathway to the superior colliculus, as measured by functional ultrasound imaging. The biosafety of the film was confirmed by the absence of short-term adverse effects under optical coherence tomography retinal imaging, while local thermal increases were measured below 1 °C. These findings demonstrate the potential of photoacoustic stimulation for high-acuity visual restoration over a large field of view in blind patients.

## Introduction

Retinitis pigmentosa and age-related macular degeneration affect millions of people worldwide[1], resulting in irreversible photoreceptor degeneration and blindness. Currently, there is no effective drug treatment for preventing photoreceptor loss. Retinal prostheses are implantable devices designed to stimulate the remaining retinal layers to restore vision[2]. To date, two retinal prosthesis designs, which both primarily use electrostimulation to restore vision, have been approved for commercial implantation[3]. However, both were later removed from the market, facing challenges such as poor spatial resolution and small restored visual field. The more recent photovoltaic-based PRIMA implant, one of the most advanced retinal prostheses currently in clinical trials (NCT04676854), offers a spatial resolution of 100 µm, and a median visual acuity below the threshold for legal blindness[4], and a limited restored visual field of 7°.

Focused ultrasound is a promising noninvasive method for retinal stimulation[5]. It has been shown to evoke stable responses in the *ex vivo* salamander retina with a 90-µm lateral resolution at 43 MHz[6] and in the *in vivo* blind RCS rat retina with a lateral resolution of around 400 µm with a 4.5-MHz transducer 2D-array[7–9]. However, it still faces safety challenges to meet FDA safety threshold for ophthalmological use[7].

Photoacoustic modulation is an emerging method for high-precision neural stimulation[10,11]. A localized ultrasound field is generated by the photoacoustic agents upon excitation with a pulsed laser, and used to stimulate neurons. High spatial resolution stimulation of single neurons has been demonstrated through a fiber-based photoacoustic emitter[10].

In this study, we investigated photoacoustic retinal stimulation as an alternative strategy for restoring vision. We here provide evidence of its efficacy both *ex vivo* and *in vivo* on healthy and degenerated retinae, as well evidence of the biosafety of the photoacoustic film in short-term implantation.

## Results

### Fabrication and characterization of the flexible photoacoustic film

The working principle of photoacoustic retinal stimulation is illustrated in Fig. 1a. A 1030-nm pulsed laser is delivered to the back of the eye onto the retina, illuminating the subretinally-implanted flexible photoacoustic (PA) film. Laser absorption by the film produces transient heating, which causes thermal expansion and compression of the material, thereby generating pulsed ultrasound. The generated ultrasound stimulates the mechanosensitive retina[6,8,12].

The PA film (Fig. 1b) is composed of candle soot (CS) as the absorber material, sandwiched between two layers of polydimethylsiloxane (PDMS), which serves as the thermal expansion material. The film has a Young's modulus of 2.12 ± 0.10 MPa to minimize the immune response[13,14] once implanted (Supplementary Fig. S1). Upon excitation with 4.2-ns laser pulses at 7 µJ per pulse, the PDMS/CS/PDMS film emitted ultrasound pulses with peak-to-peak pressure of 146.2 kPa measured 0.9 mm away (Fig. 1c). At the surface of the film, the conversion efficiency is estimated at 26 kPa.$\mu J^{-1}$ based on the distance-dependent pressure profile measured (Supplementary Fig. S2). PA signals were found to have a central frequency of 42.2 MHz and -6 dB bandwidth ranging from 29.6 to 59.9 MHz. This central frequency has been demonstrated to activate e*x vivo* salamander retinae with a lower intensity threshold compared to lower acoustic frequencies[15]. These data suggest that the PDMS/CS/PDMS film is a promising photoacoustic converter for retinal stimulation.

The spatial distribution of the ultrasound field generated by the PDMS/CS/PDMS film was further mapped by PA field microscopy (Fig. 1d). A 50-µm optical fiber was attached to the PA film to ensure a 50-µm-diameter illumination area. The axial pressure profile shows that the maximum acoustic signal is generated at the surface of the film upon illumination ($Z$ = 0 µm) and attenuates to 50% of its peak value at $Z$ = 140 µm (Fig. 1d, right). The lateral width (W) of the acoustic field, quantified by the full width at half maximum, measures W = 56 µm at Z = 0 µm and increases with axial depth to W = 124 µm at Z = 100 µm (Fig. 1e). These results confirm that under a confined illumination, the PA film produces a highly localized, 56-µm lateral ultrasound field comparable to the size of illumination, opening up potential for retinal stimulation with sub-100-µm resolution.

Measured acoustic pressure exhibited a linear relation with the incident laser energy per pulse (Fig. 1f), which indicates that the output pressure can be precisely modulated by adjusting the input laser energy.

To ensure that the laser light absorption by the designed PA film is not associated with a substantial and detrimental temperature increase, we measured the temperature at the surface of the PA film. The tested laser conditions were consistent with those employed in the following *ex vivo* retinal stimulation experiments (next section). We observed a maximum temperature rise of 0.52 ±

103 0.09 °C (Fig. 1g). The baseline change due to cumulative thermal effects was 0.21 °C after 40 s. This
104 value is an order of magnitude below the temperature increase needed for thermal neural
105 modulation[16,17]. Therefore, the film is unlikely to thermally modulate retinal neuronal activity.

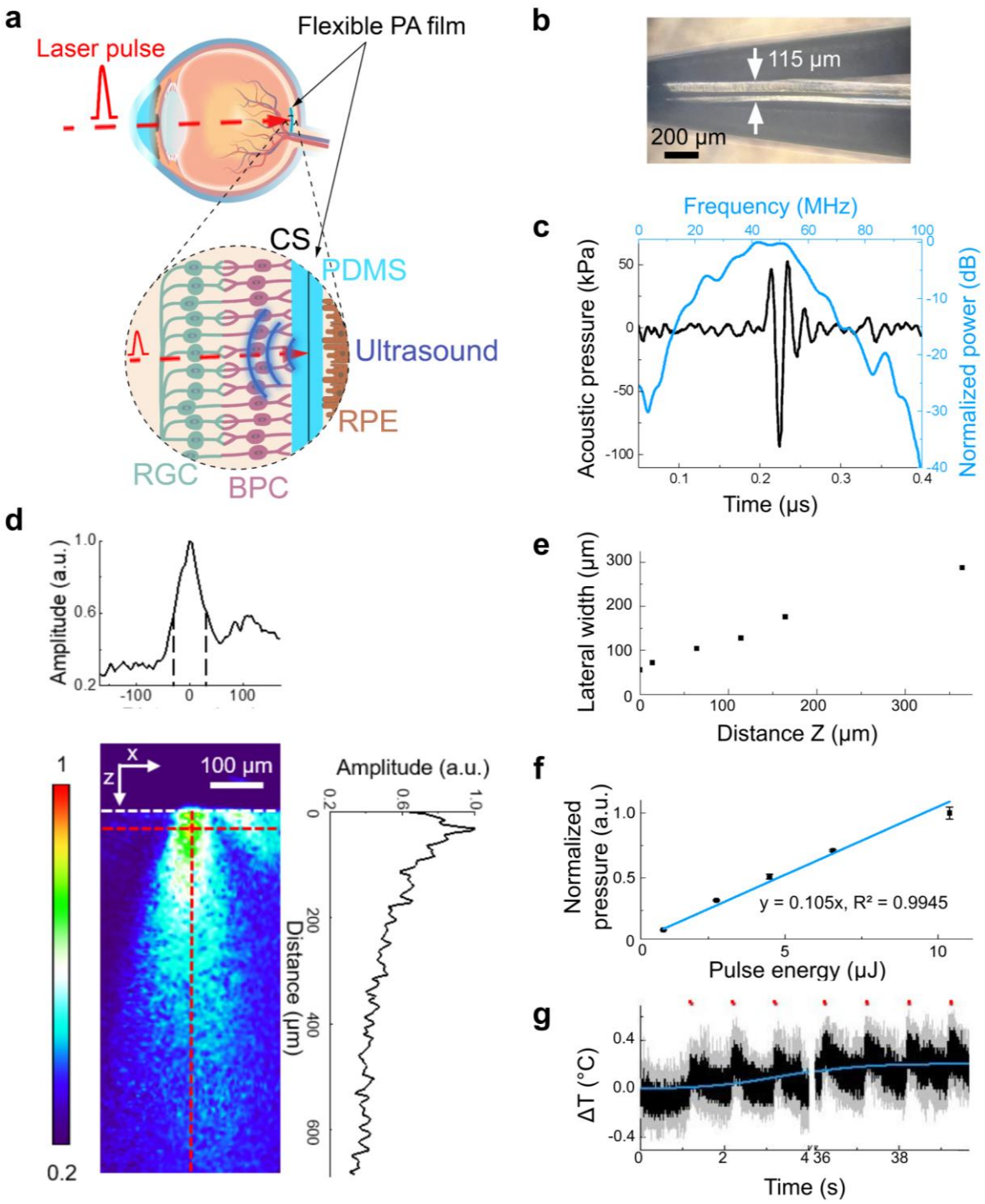


**Figure 1. Characterization of the flexible photoacoustic film. (a)** Working principle of the flexible photoacoustic (PA) film. Illumination of the PA film (cyan) with a nanosecond pulsed laser (red dashed line) produces an ultrasound emission (blue). CS: candle soot, PDMS: polydimethylsiloxane, RPE: retinal pigment epithelium, RGC: retinal ganglion cells, BPC: bipolar cells. **(b)** A photograph of the PDMS/CS/PDMS film with a three-layer design held by a tweezer. **(c)** Characterization of the PA film in the temporal domain (black) and frequency domain (blue) measured 0.9 mm away from the film

surface. **(d)** Mapping of the ultrasound field generated by the PDMS/CS/PDMS film upon illumination through a 50-µm optical fiber. *Center*: measured distribution of the generated US field. The side lobe on the right of the field is due to the slight tilted angle when the optical fiber was put in contact with the sample film. White dotted line: interface between water and the film. *Top and right*: normalized lateral and axial profiles of the PA field, respectively, measured along the red dashed lines in the center panel. The amplitude of the acoustic signal was normalized to the maximum amplitude measured in the field. **(e)** Full width at half maximum of the lateral profile as a function of the axial position *Z* extracted from (d). **(f)** Peak-to-peak pressure of the PA signal as a function of laser energy per pulse measured from a PDMS/CS/PDMS film by a hydrophone. The pressure was normalized to the maximum pressure in all measurements. N = 3 for each data point. Blue line: linear fitting: $y = 0.105x$, $R^2 = 0.9945$. **(g)** Temperature increase at the surface of the PA film following illumination with a 200-µm laser spot. N = 3 for each data point, mean (black line) ± SD (gray shade). Red dots: laser on. Laser parameters: energy of 10 µJ per pulse, repetition rate of 3 kHz (laser power density $P = 0.95$ W/mm²), and burst duration 50 ms, delivered every 1 s over 40 s. The baseline change due to cumulative thermal effect was obtained by logistic curve fitting to the data (blue line).

129 **Photoacoustic modulation of the *ex vivo* retina**

130 To evaluate retinal responses following photoacoustic stimulation, we recorded the activity
131 of retinal ganglion cells (RGCs) from *ex vivo* retinae of wild-type Long-Evans (LE) rats on a multi-
132 electrode array (n = 4 rats). The PDMS/CS/PDMS film was placed on the *ex vivo* retina against the
133 photoreceptor layer. It was photoactivated by a 1030-nm pulsed laser delivered through a 200-µm
134 optical fiber (Fig. 2a), which was successively moved at different positions between stimulations. We
135 applied 4.2-ns laser pulses at a repetition rate of 1.9 kHz (every 520 ns) for a burst duration of $d_b$ = 10
136 ms, with a pulse energy of 10 µJ (Fig. 2b, top; power density P = 0.27 $W.mm^{-2}$), yielding an estimated
137 peak-to-peak ultrasound pressure of 0.12 MPa.

138 Photoacoustic stimulation evoked robust RGC responses in healthy LE retinae (Fig. 2b, 2c, top
139 two panels). Individual RGCs were considered responsive or modulated if their firing rate significantly
140 increased (excited response) or decreased (inhibited response) relative to baseline (Fig. 2c, 2e). 100
141 LE RGCs (78%) exhibited an alteration in activity upon PA stimulation (Fig. 2e) out of the 129
142 spontaneously active RGCs on the electrodes contained in a 300-µm-radius area centered on the laser
143 spot. Responsive RGC activity was mainly increased (92% of responding RGCs, Fig. 2d, left). RGCs with
144 an increased activity had a mean response firing rate of 66 ± 3.7 Hz (Fig. 2f), and had a mean response
145 latency of 51 ± 34.2 ms (Fig. 2g). The response latency was inversely correlated with the firing rate
146 (Fig. 2h).

147 To investigate the potential of such photoacoustic stimulation for restoring vision, we then
148 stimulated *ex vivo* retinae from blind P23H rats (n = 4 rats). Similarly to LE retinae, though with a lower
149 fraction, 89 out of 229 P23H RGCs (39%) exhibited robust responses to photoacoustic stimulation (Fig.
150 2c-e), predominantly with increased activity (93% of responding RGCs). Compared to LE RGCs, P23H
151 RGC firing rate was significantly lower following stimulation (29 ± 2.88 Hz, Fig. 2f) and response latency
152 was significantly increased (89 ± 65 ms, Fig. 2g). Only 36% of P23H RGCs had response latencies below
153 45 ms[12], which was significantly fewer than LE cells (39%, Fig. 2g). The reduction in short-latency
154 responses suggests that photoreceptors may partly contribute to this early retinal
155 mechanosensitivity[6,18]. These results on the P23H rat retina demonstrate the *ex vivo* efficacy of
156 photoacoustic stimulation in modulating retinal ganglion cells activity in degenerated retinae.

157 To further define the origin of the PA responses, we bath-applied glutamatergic blockers (rs)-
158 CPP and CNQX to P23H retinae (Fig. 2i). PA-induced responses were nearly completely abolished, and
159 recovered following the washout of the blockers (Fig. 2i). These results suggest that the main
160 mechanosensitive cells are upstream of RGCs, consistent with previous studies[6,12,18,19], and that
161 glutamate neurotransmission is required to transfer the mechanosensitive signal to the RGCs.

To exclude the possibility that the healthy LE retina was responding to the pulsed laser light[20,21], we performed off-film stimulation by applying laser pulses to the bare LE. Using identical laser conditions, only 3.6 ± 0.9% of RGCs showed a modified activity following off-film stimulation, compared to 77 ± 20% following on-film photoacoustic stimulation (Fig. 2j). Furthermore, we found that the PA film absorbs more than 99% of the on-film applied laser energy (Supplementary Fig. S3). These results confirm that the observed RGC responses upon laser activation of the photoacoustic film were not caused by a direct light activation of the healthy retina.

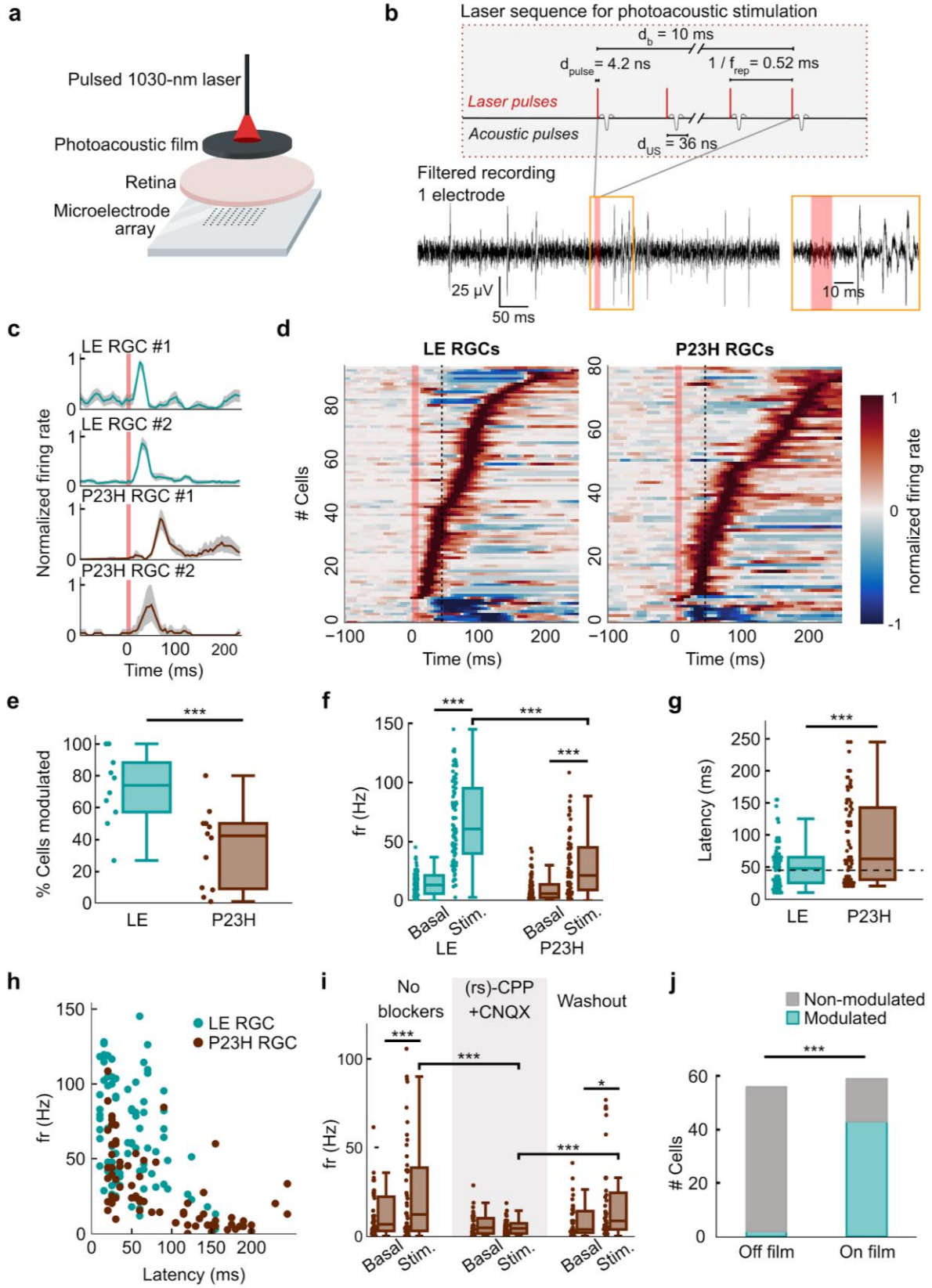
a
Pulsed 1030-nm laser
Photoacoustic film
Retina
Microelectrode array
b
Laser sequence for photoacoustic stimulation
d_b = 10 ms
d_pulse = 4.2 ns
1 / f_rep = 0.52 ms
Laser pulses
Acoustic pulses
d_US = 36 ns
Filtered recording
1 electrode
25 µV
50 ms
10 ms
c
LE RGC #1
LE RGC #2
P23H RGC #1
P23H RGC #2
Normalized firing rate
Time (ms)
d
LE RGCs
P23H RGCs
# Cells
Time (ms)
normalized firing rate
e
% Cells modulated
LE
P23H
f
fr (Hz)
Basal
Stim.
LE
P23H
g
Latency (ms)
LE
P23H
h
LE RGC
P23H RGC
fr (Hz)
Latency (ms)
i
No blockers
(rs)-CPP +CNQX
Washout
fr (Hz)
Basal
Stim.
j
Non-modulated
Modulated
# Cells
Off film
On film

**Figure 2. Photoacoustic modulation of *ex vivo* wild type and degenerated retinae. (a)** The *ex vivo* retina was placed on a multi-electrode array (MEA) with the photoacoustic film on the outer layer. **(b)** *Top*: schematic of the laser sequence for photoacoustic stimulation. Laser pulses, with an energy of $E_p$ = 10 µJ per pulse and duration $d_{pulse}$ = 4.2 ns, were delivered at a repetition frequency $f_{rep}$ = 1.9 kHz during a single burst of duration $d_b$ = 10 ms. Each laser pulse is converted by the PA film into an acoustic wave with a duration $d_{US}$ = 36 ns. *Bottom*: Example high-pass filtered MEA recording from a single electrode displaying elicited spikes following a photoacoustic stimulation. Red shaded area: laser on. Inset: zoom in of action potentials following stimulation. **(c)** Examples of Long Evans (LE) and P23H RGC responses to photoacoustic stimulation. Cyan (LE) and brown (P23H) lines: mean firing rate. Gray shaded areas: 99% bootstrapped CI from 1000 samples. Red shaded area: PA stimulation. **(d)** Heatmaps of normalized firing rates for responsive LE RGCs (left, n = 100) and P23H RGCs (right, n = 88). Red shaded area: PA stimulation. Dashed black line: 45-ms cutoff for slow and fast latency responses. Cells with excited responses display an increase in firing rate after photoacoustic stimulation (red), and cells with inhibited responses display a decrease in firing rate (blue). **(e)** Percentage of cells modulated by photoacoustic stimulation per stimulation site. LE: 74% (4 rats, n = 10 stimulation sites), P23H: 39 %, (4 rats, n = 12 stimulation sites). *** $p < 0.001$, Mann Whitney U test. **(f)** Firing rates of LE and P23H RGCs during baseline (basal) and following stimulation (stim). Mean firing rates: LE: $fr_{basal}$ = 14 ± 1.0 Hz, $fr_{stim}$ = 66 ± 3.7 Hz (n = 82 RGCs within stimulation range, $p < 0.001$, Wilcoxon signed-rank); P23H: $fr_{basal}$ = 10 ± 1.2 Hz, $fr_{stim}$ = 29 ± 2.88 Hz (n = 72 RGCs within stimulation range, $p < 0.001$, Wilcoxon signed-rank). **(g)** Latencies of RGC responses for LE (51 ms ± 34.2 ms, mean ± standard deviation) and P23H (89 ms ± 65 ms). Dashed black line: 45-ms cutoff for slow and fast latency responses. **(h)** Firing rate of modulated RGCs as a function of response latency. Firing rate and response latency of excited RGCs were correlated for LE ($r = -0.40$, $p < 0.001$, Pearson correlation) and P23H ($r = -0.59$, $p < 0.001$, Pearson correlation) RGCs. **(i)** Glutamate blockers (rs)-CPP and CNQX abolished RGC responses to photoacoustic stimulation in P23H retinae. The population firing rate of RGCs (n = 44 cells, 2 retinae) is compared between baseline (basal) and stimulation (stim), before blocker admission (no blocker), following blocker admission ((rs)-CPP+CNQX) and after washout (washout) with Ringer medium. Firing rates per condition, *no blockers*: $fr_{basal}$ = 12 ± 13 Hz, $fr_{stim}$ = 26 ± 29 Hz ($p < 0.001$); (rs)-*CPP+CNQX*: $fr_{basal}$ = 6 ± 6 Hz, $fr_S$ = 6 ± 4 Hz ($p$ =0.749); *washout*: $fr_{basal}$ = 8 ± 9 Hz, $fr_{stim}$ = 21 ± 27 Hz ($p$ = 0.021). Comparison of the population stimulation firing rate $fr_{stim}$ after blocker admission and $fr_{stim}$ before admission ($p < 0.001$, Wilcoxon signed-rank), and $fr_{stim}$ after washout ($p < 0.001$, Wilcoxon signed-rank). **(j)** Off-film laser light stimulation. Percentage of LE RGCs modulated by direct laser stimulation on the retina ("off film") compared to photoacoustic stimulation ("on film"). Laser parameters: $E_p$ = 10 µJ per pulse, $f_{rep}$ = 3.5 kHz, $d_b$ = 10 ms. Off film: 3.6% ± 0.9% (n = 56 cells, 2

205 retinae), on film: 77% ± 20% (n = 59 cells, 3 retinae). Statistics: * $p < 0.05$, *** $p < 0.001$, Mann-Whitney
206 U test.

207 **Dependence of RGC response on laser conditions**

208 We further investigated RGC responses to photoacoustic stimulation using different laser
209 repetition rates (10 µJ per pulse, $f_{rep1}$ = 1.9 kHz with $P_1$ = 0.27 mW.mm$^{-2}$ and $f_{rep2}$ = 3.5 kHz with $P_2$ =
210 0.52 mW.mm$^{-2}$) and burst durations ($d_b$ = 5 - 30 ms). In LE retinae, the firing rates of cells with excited
211 responses increased with burst durations up to $d_b$ = 25 ms for $f_{rep1}$, while at $f_{rep2}$ they plateaued up to
212 $d_b$ = 15 ms and decreased with longer burst durations (Fig. 3a-b, left). P23H RGCs with excited
213 responses also showed an increase in firing rate with longer burst durations for $f_{rep1}$ (Fig. 3a-b, right),
214 while firing rate increased for burst durations up to $d_b$ = 20 ms then decreased with longer burst
215 durations for $f_{rep2}$ (Fig. 3b, right). LE RGC firing rates were significantly higher than those for P23H
216 RGCs, up to 2.8-fold during $d_b$ = 25 ms and up to 4.7-fold during $d_b$ = 20 ms with $f_{rep1}$ and $f_{rep2}$,
217 respectively (Fig. 3b). These results suggest that the degenerated retina requires higher thresholds for
218 photoacoustic stimulation, consistent with previous findings concluding on a higher acoustic
219 stimulation threshold in degenerated retinae compared to wild-type retinae[8]. LE RGC response
220 latencies did not increase with burst duration or repetition rate (Fig. 3c), nor did P23H RGC latencies.

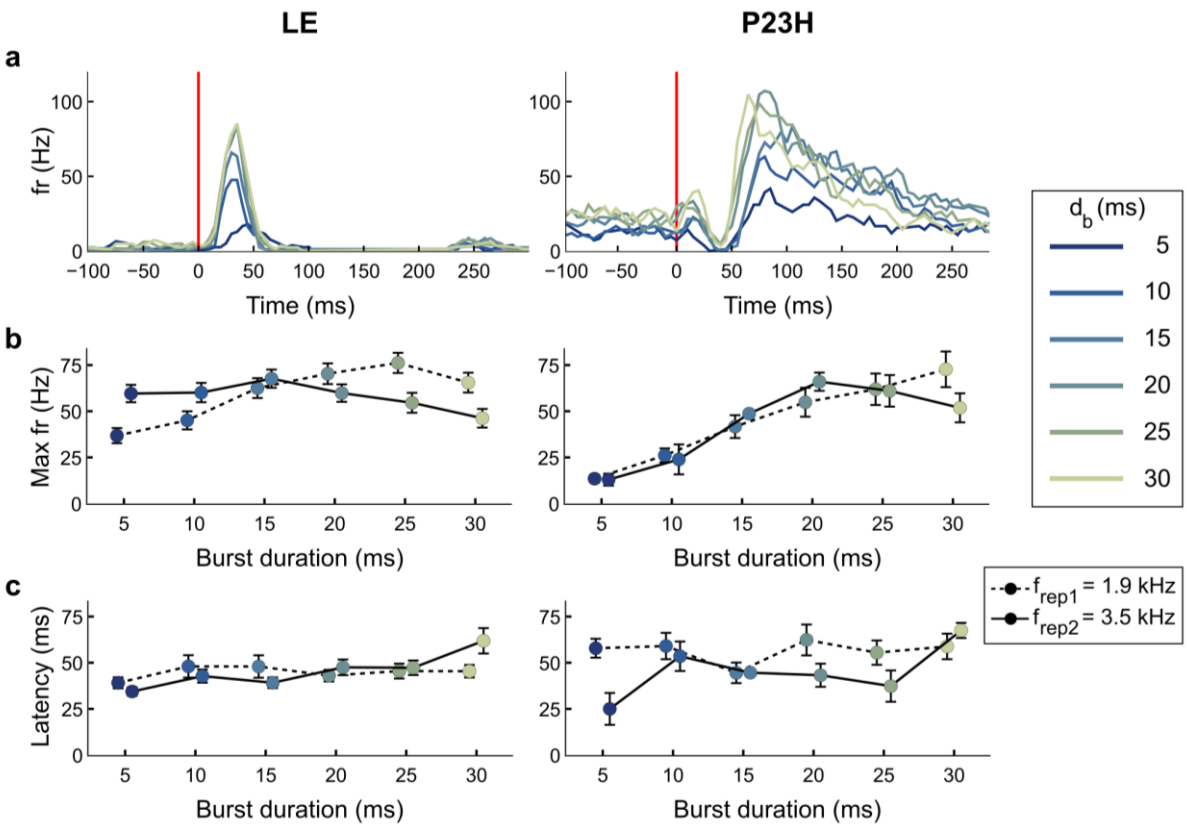


**Figure 3. RGC responses under different laser burst durations and laser repetition rates. (a)** Example LE (left) and P23H (right) cells showing increased maximum firing rate (fr) with increased burst duration (recorded at $f_{rep1}$ = 1.9 kHz). Lighter colors indicate longer burst durations ($d_b$= 5-30 ms). Vertical red lines: laser onset. **(b)** Maximum firing rate as a function of burst duration for LE and P23H RGCs during stimulation with repetition frequencies $f_{rep1}$ = 1.9 kHz (dashed line) and $f_{rep2}$ = 3.5 kHz (solid line). Data are plotted as mean + SE. In LE RGCs (left panel), the firing rate was positively correlated with burst duration for $f_{rep1}$ (r = 0.91, p = 0.01, Pearson R). In P23H RGCs (right panel), the firing rate was positively correlated during both $f_{rep1}$ (r = 0.996, p < 0.001) and $f_{rep2}$ (r = 0.811, p = 0.05). With $f_{rep1}$, for $d_b$ = 5 ms and 20 ms, the maximum firing rate of LE RGCs was 2.8- and 1.3-fold higher, respectively, than for P23H RGCs (p < 0.001 for all conditions, Mann-Whitney U-test). With $f_{rep2}$, for $d_b$ = 5 ms, the maximum firing rate of LE RGCs is 4.7-fold higher than for P23H RGCs (p < 0.001, Mann-Whitney U-test). **(c)** Response latency as a function of burst duration for LE and P23H RGCs showed no significant correlation (LE: p = 0.70 and p = 0.19 for $f_{rep1}$ and $f_{rep2}$, respectively; P23H: p = 0.79 and p=0.61, Pearson R). In both (b) and (c), dashed lines: $f_{rep1}$ = 1.9 kHz ($P_1$ = 0.27 W.mm$^{-2}$). Solid lines: $f_{rep2}$ = 3.5 kHz ($P_2$ = 0.52 W.mm$^{-2}$). Dataset for (b) and (c): for LE, n = 244 cells, recorded from 4 retinae. For P23H, n = 104 cells, recorded from 4 retinae.

240 **Spatial resolution of *ex vivo* photoacoustic retinal stimulation**

241 To investigate the spatial resolution of the photoacoustic retinal stimulation, we sequentially
242 targeted multiple positions on the film by moving the laser-delivering 200-µm fiber at different sites
243 above the photoacoustic film and mapped the responsive retinal cells (Fig. 4a). The laser repetition
244 rate was set at $f_{rep1}$ = 1.9 kHz for LE retinae (n = 11 sites) and $f_{rep2}$ = 3.5 kHz for P23H retinae (n = 6
245 sites), to account for the higher modulation threshold previously described for P23H retinae.

246 To assess the spatial distribution of PA-modulated RGCs with excited responses, we mapped
247 the maximum RGC firing rate relative to the stimulation site (Fig. 4b). For both LE and P23H RGCs, the
248 maximum firing rates were located within an area slightly larger than the laser spot (< 400 µm from
249 center), and were negatively correlated with the distance from the laser spot (Fig. 4c). Furthermore,
250 the percentage of responsive RGCs decreased when increasing the distance from the center of the
251 laser spot (Fig. 4d). 73% of LE RGCs and 70% of P23H RGCs were modulated within a 100-µm distance,
252 compared to 14% of LE RGCs and 6% of P23H RGCs at a 400-µm distance. These results indicate that
253 stimulation with the PA film induces a localized response and demonstrate the potential for a high
254 spatial resolution in photoacoustic stimulation.

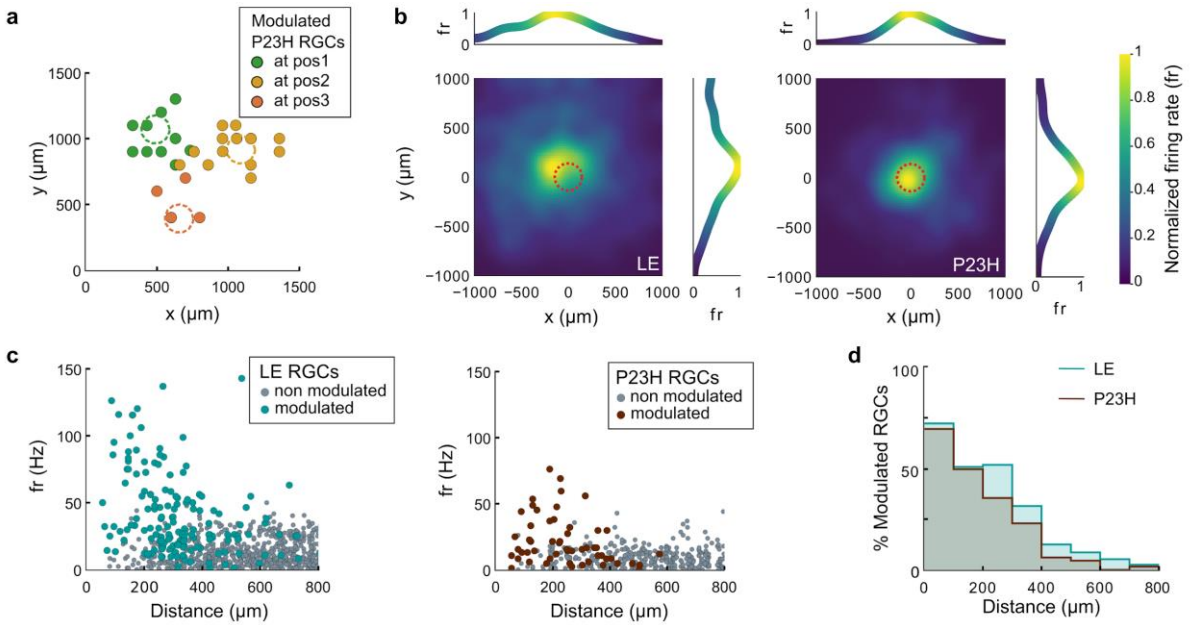


**Figure 4. Spatial distribution of RGC modulation upon photoacoustic stimulation. (a)** Different populations of RGCs were modulated by moving the laser fiber at different sites on the film. Example of a P23H retina stimulated at three sites; modulated cells at each stimulation site are grouped by color. The 300-µm-diameter laser spots are marked by dashed circles. **(b)** RGC firing rate of modulated cells normalized to maximum firing rate, mapped relative to the stimulation site for LE (left, 4 retinae, 11 stimulation sites) and P23H (right, 4 retinae, 6 stimulation sites). RGC maximum firing rates were averaged across all recorded cells at the same XY coordinates relative to the center of the laser spot (LE: n = 576 and P23H: n = 157 RGCs). Dashed circle: 300-µm-diameter laser spot. The shift between the maximum firing rate and the laser spot may be due to uncertainty in the laser spot coordinates, due to the 100-µm pitch of the MEA used for indirect measurement of the exact laser position. **(c)** Maximum firing rate for individual cells as a function of distance from the laser for LE (left) and P23H (right) RGCs. The response firing rate is negatively correlated with distance (LE: $r = -0.310$, $p < 0.001$. P23H: $r = -0.268$, $p < 0.05$, Pearson R). Each circle represents an individual cell. Cyan and brown: LE and P23H RGCs modulated by photoacoustic stimulation, respectively. Gray: non-modulated cells. **(d)** Percentage of RGCs modulated as a function of distance from the laser spot. Cyan: LE cells. Brown: P23H cells. Datasets for (c) and (d) are the same as for (b).

## *In vivo* safety of the photoacoustic implants

To test the feasibility of photoacoustic stimulation and the biosafety of the film *in vivo*, we chronically implanted 1-mm-diameter PA films in LE and P23H rats. Two designs of PA films were used for *in vivo* experiments. The 115-µm-thick PDMS/CS/PDMS film, used in the previous *ex vivo* experiments, was optimized for high photoacoustic conversion efficiency and easy handling. A thinner 40-µm-thick uniformly mixed PDMS-CNT film (characterized in Supplementary Fig. S4) was designed to approach the 30-µm thickness of the clinically tested PRIMA photovoltaic implant, which has shown no long-term adverse effects aside from minor retinal thinning in patients[4].

After implantation, eye fundus imaging confirmed the correct positioning of the implant near the optic nerve and the overall integrity of the retina (Fig. 5a-b). No complications, such as retinal tearing after implantation or major inflammation after 7 days post-implantation (dpi), were observed on the OCT images and eye fundus exams. Although the presence of glial cells between the implant and the retina is expected, stimulation efficacy should not be affected, as acoustic attenuation is below 10 $dB.mm^{-1}$ [22].

On OCT, the average retinal thickness was 174.0 ± 2.3 µm for LE rats (n = 13) and 72.3 ± 2.3 µm for degenerated P23H rats (n = 8). At the PDMS/CS/PDMS implant position, LE retinal thickness decreased to 123.2 ± 2.9 µm at 15 dpi, 121.5 ± 4.2 µm at 30 dpi, and 107.3 ± 2.0 µm at 90 dpi (Fig. 5c). In LE rats implanted with the PDMS-CNT implant, similar values of 113.0 ± 4.8 µm at 15 dpi and 105.8 µm at 30 dpi, were measured (Fig. 5c). The decrease in the retinal thickness above the implant in LE rats was due to photoreceptor degeneration (Fig. 5a, right), caused by the physical separation of photoreceptors from the retinal pigment epithelium, as previously reported with other prostheses[23,24]. In implanted P23H rats, retinal thickness above the implant remained stable and comparable to the neighboring area for up to four months for both PDMS/CS/PDMS and PDMS-CNT implants (Fig. 5d). These observations indicate that the photoacoustic implants have no intrinsic short-term toxicity on the wild-type and degenerated retinae.

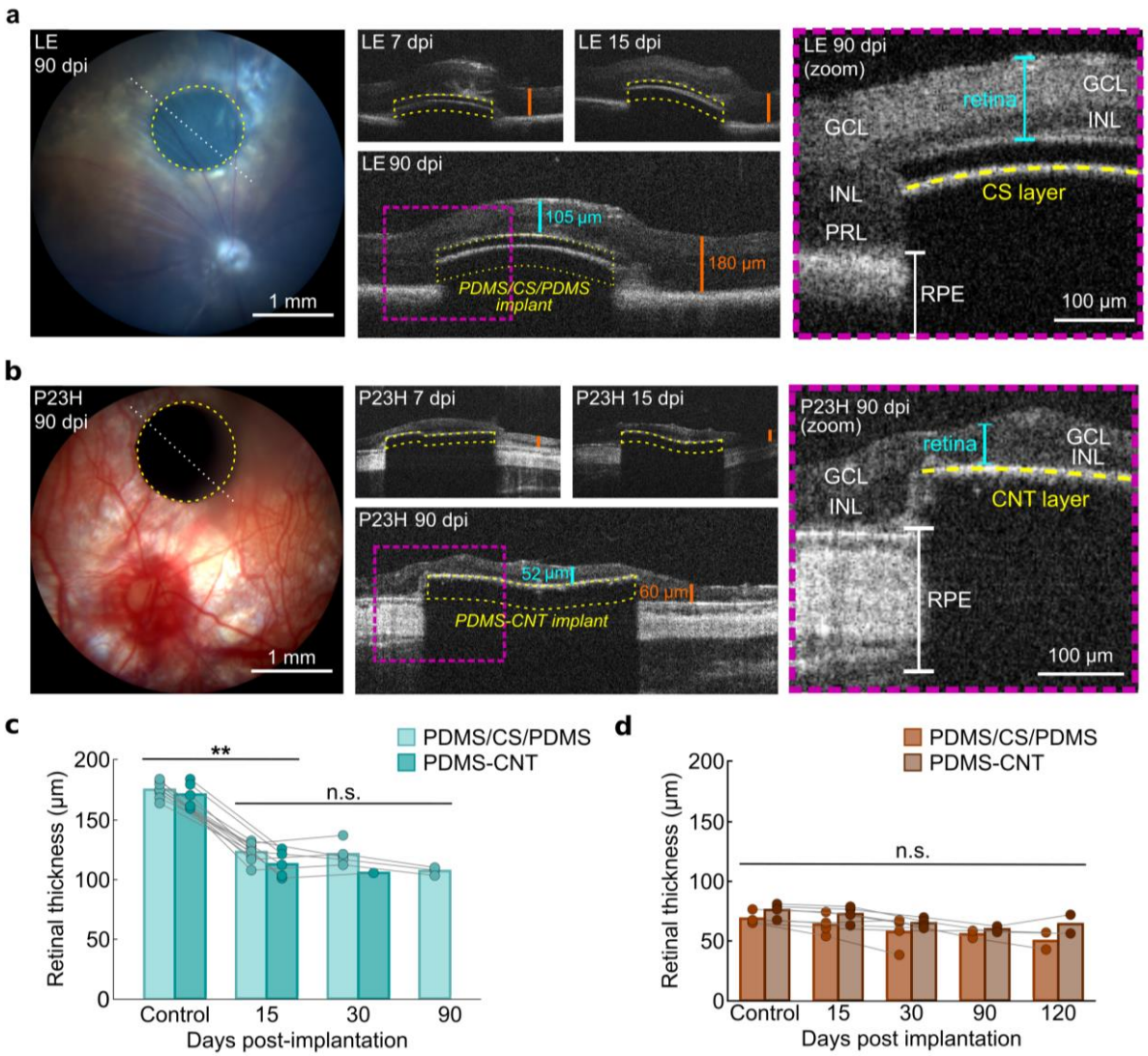


**Figure 5. *In vivo* photoacoustic implant biocompatibility. (a)** Eye fundus (left) and OCT images (middle and right) of an LE rat retina with a subretinal PDMS/CS/PDMS implant (yellow dotted line) at 7, 15, and 90 days post-implantation (dpi). OCT images were taken along the white dotted line shown in the left panel. In the zoomed-in OCT images, GCL: retinal ganglion cell layer, INL: inner nuclear layer, PRL: photoreceptor layer. RPE: retinal pigmented epithelium. The PR layer has degenerated above the implant. Right inset: zoom on the OCT image at 90 dpi. **(b)** Same as (a) but for a P23H rat. **(c)** Mean LE retinal thickness above PDMS/CS/PDMS (light cyan) and PDMS-CNT (dark cyan) implants over time. Control: mean retinal thickness next to the implant at 15 dpi. Thickness at 15 dpi and later is significantly lower than control thickness (**$p < 0.01$, Wilcoxon Signed-Rank test). At 15 dpi, the thickness above PDMS/CS/PDMS implants is not statistically different from the thickness above PDMS-CNT implants ($p = 0.16$, Mann-Whitney U test). Between 15 dpi and 90 dpi, the decrease in thickness above PDMS/CS/PDMS implant (123.2 ± 2.9 µm to 107.3 ± 2.0 µm) is not significant ($p = 0.25$, Wilcoxon

Signed-Rank test). **(d)** Same as (c) for P23H rats. The difference of retinal thickness above both implants is not statistically significant ($p = 0.16$ at 15 dpi and 0.32 at 30 dpi, Mann-Whitney U-test). Retinal thickness is stable up to 120 dpi for both PDMS-CNT ($p = 0.18$, one-way ANOVA) and PDMS/CS/PDMS implants ($p = 0.51$).

316 **Photoacoustic retinal stimulation *in vivo***

317 We then examined *in vivo* photoacoustic stimulation of the degenerated retina using
318 subretinal PDMS/CS/PDMS and PDMS-CNT implants in LE rats. As indicated above, photoreceptors
319 degenerate above the implant in LE rats, creating a localized model of retinal degeneration at the
320 photoacoustic stimulation site (Fig. 5a, c). Activation of the visual pathway was assessed in the
321 contralateral Superior Colliculus (cSC) using functional ultrasound imaging (fUS), which measures
322 relative changes in cerebral blood volume (rCBV) triggered by neuronal excitation (Fig. 6a). To verify
323 the coordinates of the cSC, we measured its activation using control full-field white light stimulation
324 of the implanted eye (P = 0.02 $mW.mm^{-2}$). This generated a large rCBV response area in the cSC (Fig.
325 6c, i), which was used as a reference area in further analyses (Fig. 6f). We measured a large increase
326 in the amplitude of the rCBV, averaged on a 29-by-29-pixel (29 pixels = 302 ± 10 µm) square region of
327 interest (ROI; Fig. 6f, light gray), which was centered on the maximum responses in the cSC. The same
328 ROI was subsequently used to compute the averaged rCBV for all of the stimulation conditions (Fig.
329 6f). To better define the expected size of the activated area for PA stimulation, we focused a 400-µm-
330 diameter spot of 595-nm laser light (P = 0.21 $mW.mm^{-2}$) onto the healthy retina next to the implant
331 (Fig. 6b, iii). It similarly triggered an increase in rCBV in the cSC (Fig. 6c, ii), with an activated area
332 representing 32 ± 11 % (n = 6) of the area activated by the full-field white light (Fig. 6f). In the same
333 29-by-29-pixel ROI, the rCBV amplitude and response kinetics were similar to those generated by the
334 full-field white light stimulation (Fig. 6g, orange).

335 We then proceeded with photoacoustic stimulation on the implants (Fig. 6b, ii; Fig. 6d, top).
336 The 1030-nm laser delivered eight 125-ms bursts during 2 s, repeated every 15 s, for a total of 15
337 stimulations per recording (Fig. 6d). Laser power densities were P = 0.29 ± 0.06 $W.mm^{-2}$ (mean ± SD)
338 for PDMS/CS/PDMS implants and P = 0.39 ± 0.12 $W.mm^{-2}$ for PDMS-CNT implants. The estimated peak-
339 to-peak acoustic pressures at the surface of the implants were 0.05 MPa and 0.15 MPa for
340 PDMS/CS/PDMS and PDMS-CNT implants, respectively. We observed activation in a large cSC area
341 following each photoacoustic stimulation (Fig. 6d-e) using both types of implants (Fig. 6c, iii).
342 Photoacoustic stimulation with the PDMS/CS/PDMS and PDMS-CNT implants activated cSC areas
343 measuring 25 ± 4 % (n = 4) and 38 ± 10 % (n = 5) of the full-field-white-light-activated area, respectively
344 (Fig. 6f). Furthermore, in the 29-by-29-pixel ROI, the averaged rCBV amplitudes for the
345 PDMS/CS/PDMS (Fig. 6g, blue) and PDMS-CNT (Fig. 6g, black) implant stimulations reached similar
346 amplitudes to that generated with the 400-µm-diameter spot of the 565-nm laser light on the healthy
347 retina (Fig. 6g, orange). The size of the activated areas generated by stimulation with the
348 PDMS/CS/PDMS and PDMS-CNT implants, and with the 595-nm-laser spot, were not significantly
349 different (Fig. 6f). By contrast, a direct 1030-nm-light stimulation of the healthy retina (Fig. 6c, iv; P =

350 0.56 ± 0.21 W.mm$^{-2}$, 400-µm-diameter spot) did not generate a significant cSC activation (Fig. 6f). The
351 averaged rCBV was negligible in the ROI, and statistically different from all of the other measurements
352 (Fig. 6g, dark red). Taken together, these results show that the photoacoustic stimulation of the
353 degenerated retina elicits a robust and local activation of the visual pathway downstream of the
354 retina, with an amplitude and size comparable to a visible light stimulation of the retina.

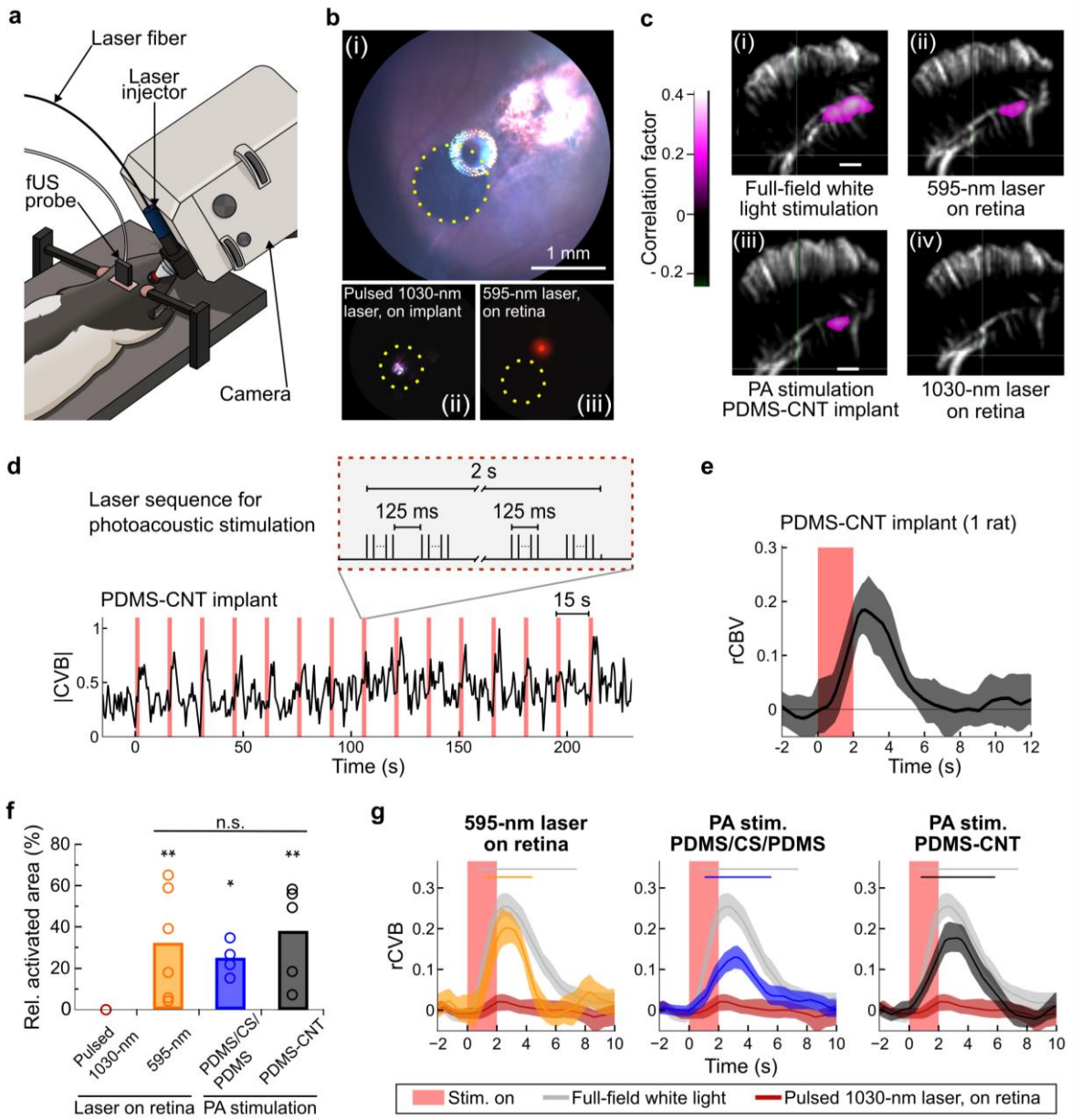


**Figure 6. Superior colliculus activation following photoacoustic stimulation of *in vivo* LE retinae. (a)** Setup for *in vivo* eye stimulation and fUS recordings. **(b)** Eye fundus images of a 1-mm PA implant (*i,* yellow dotted circle) and 400-µm-diameter laser spots (*ii*: pulsed 1030-nm laser on the implant, *iii*: continuous 595-nm laser on the retina) used for laser and photoacoustic stimulation. **(c)** Functional ultrasound imaging in the coronal plane (left hemisphere, AP, -6.5 mm from the bregma). The correlation map displays the relationship between relative cerebral blood volume (rCBV) and the stimuli. Active pixels reflect regions of activated neurons in the contralateral superior colliculus (cSC) for a single recording (15 stimulations). **(d)** Top: Laser sequence for photoacoustic stimulation (repetition rate $f_{rep}$ = 6.1 kHz). Bottom: example normalized CBV trace for pulsed 1030-nm

photoacoustic stimulation on a PDMS-CNT implant (measured in 29-by-29-pixel region of interest of the cSC). **(e)** Average rCBV for a single session with 15 stimulations (same data as for (d)). Mean rCBV ± 99% CI. Red shaded area: PA stimulation. **(f)** Activated area following stimulation, relative to the area activated by full-field white light stimulation (rel. activated area), for different stimuli: full-field white light stimulation (light gray, 6 rats, n = 6 recordings), 1030-nm laser stimulation on the retina (dark red, 3 rats, n = 4 recordings), 595-nm laser stimulation on the retina (orange, 3 rats, n = 6 recordings), photoacoustic stimulation with PDMS/CS/PDMS implant (blue, 3 rats, n = 4 recordings), and photoacoustic stimulation with PDMS-CNT implant (black, 2 rats, n = 5 recordings). The activated area is measured by counting the number of pixels on correlation maps such as (c). Circles on the graph mark the ratio for individual recordings. Statistics: p-values vs white light stimulation: * $p < 0.05$, ** $p < 0.01$, Wilcoxon Signed-Rank test. PDMS/CS/PDMS vs 595 nm: $p = 0.91$, PDMS-CNT vs 595 nm: $p = 0.792$, PDMS/CS/PDMS vs PDMS-CNT: $p = 0.56$, Mann-Whitney U test. **(g)** Mean rCBV responses of individual rats following stimulation with a laser (595-nm and 1030-nm on retina) and photoacoustic stimulation, for all rats. Same data as (f). Horizontal bars denote significant elevation with respect to the baseline (e.g., no overlap of CI with basal CI). No significant difference in rCVB following photoacoustic stimulation between both implant types was found (e.g., overlapping confidence intervals). Peak rCBV values: white light, 0.26 (at 2.65 s); 595 nm, 0.20 (at 2.69 s); PDMS-CNT, 0.18 (at 3.24 s); PDMS/CS/PDMS, 0.13 (at 3.18 s); 1030-nm laser on retina, 0.02 (at 2.19 s). Shaded areas: 95% bootstrapped CI. Red shaded area: PA stimulation.

## Discussion

In this study, we developed flexible photoacoustic films that efficiently generated acoustic waves. The generated photoacoustic waves successfully stimulated the activity of retinal cells *ex vivo* and *in vivo*, thereby activating downstream visual pathways *in vivo*. This RGC stimulation was demonstrated both *ex vivo* and *in vivo* on degenerated retinae. These results therefore provide evidence that the degenerated retina maintains some ultrasound sensitivity, enabling RGC activity modulation and the consecutive stimulation of higher visual areas for visual restoration.

We showed that an acoustic pressure of 0.05 MPa was sufficient to elicit responses in the superior colliculus, which is two orders of magnitude lower than the pressure thresholds previously reported for *in vivo* transducer-based ultrasound retinal stimulation[9]. Pressure thresholds of photoacoustic stimulation correspond to mechanical indexes (MI) below 0.03 (PDMS/CS/PDMS film) and 0.1 (PDMS-CNT film) and spatial peak temporal average intensities ($I_{SPTA}$) below 0.06 and 0.9 $mW.cm^{-2}$, respectively (Supplementary Table T1). Temperature increases were measured to be below 1 °C at the film surface (Fig. 1g, Supplementary Fig. S6). These metrics align with FDA safety guidelines for ultrasonic ophthalmic devices[25], making our PA implants a promising option for safe ultrasound stimulation of the retina.

Restoring meaningful vision requires high spatial resolution over a large area of the retina. To achieve this, each individual stimulation source (pixel) must produce tightly confined fields with sub-20-µm[26] lateral resolution, and maximize pixel density to 2500 $px.mm^{-2}$ in the macula, which covers a 25 $mm^2$ area in humans. Among current electrical retinal prostheses, complex 3D honeycomb photovoltaic devices[27] and optimized laser stimulation sequences[28] show potential to generate 20-µm-wide electric fields with dense arrays of thousands of electrodes, but each rigid implant can only cover at best 9 $mm^2$ of the retina. Ultrasound retinal stimulation offers the advantage of non-invasive stimulation over an area greater than the macula, but the pixel density of transducer 2D-arrays is very limited (currently 16 x 16[9]) regardless of the lateral resolution of the stimulation field, which remains above 80 µm (*in silico* data, at 20 MHz[9]). The photoacoustic film demonstrated in this study offers the potential to meet both of these needs due to its spatially continuous nature and the multiplexing capability of photons. We demonstrated that a 50-µm-diameter laser spot generates a 56-µm lateral ultrasound field, and that the RGC activity was locally modulated around the laser spot in both healthy and degenerated retinae. The potential of the photoacoustic film to enable high visual acuity using smaller laser spot sizes is currently under investigation. Moreover, the pixel number could exceed a million by using digital micromirror devices to project a laser pattern onto the continuous film.

While further studies are required to investigate the mechanisms of photoacoustic retinal stimulation and whether the implant can restore meaningful vision to patients afflicted by retinal

degenerative diseases, our results collectively demonstrate that photoacoustic retinal stimulation through flexible implants opens up potential for an innovative strategy for restoring vision, with high precision and a large field of view.

423 # Material and methods

424 ## Design of the photoacoustic film

425 The laser wavelength and the PA materials were both optimized for safety and performance. Light
426 wavelengths ranging from 500 nm to 1150 nm have maximum transmission in the human eye media[29].
427 A nanosecond laser with a 1030-nm wavelength was chosen to maximize transmission to the retina[29],
428 while avoiding triggering responses in photoreceptors, as AMD patients may retain peripheral vision.
429 CS and CNT were selected as the absorber material due their high photoacoustic conversion efficiency,
430 accessibility, and lower safety concerns compared to lead-containing materials[30,31]. For the thermal
431 expansion material, PDMS was identified as the best option due to its transparency, high Grüneisen
432 parameter, excellent biocompatibility, and stability[32]. The PDMS mixing ratio was adjusted to 5:1 to
433 increase the Young's modulus, thereby enhancing photoacoustic conversion efficiency[33].
434

435 ## Fabrication of the photoacoustic films

436 To fabricate the 115-µm-thick PDMS/CS/PDMS film, a uniform layer of candle soot was flame-
437 synthesized and deposited onto a glass slide for 20 s, achieving a thickness of approximately 4 µm.
438 Subsequently, a degassed PDMS mixture of silicone elastomer base and curing agent (Sylgard 184,
439 Dow Corning Corporation, USA) with mix ratios of 5:1 was spin-coated at 500 rpm onto the candle
440 soot layer, and cured at 110 °C for 15 minutes. The resulting cured film was then detached from the
441 glass slide, inverted, and reattached. Another layer of PDMS mixture was spin-coated at 500 rpm and
442 cured at 110 °C for 15 minutes. Both sides of the film were treated with oxygen plasma for 1 min to
443 make the implant surface hydrophilic[34]. The film was cut into smaller areas (5 x 5 $cm^2$) and stored in
444 distilled water before use to avoid reversion to their hydrophobic state. Biopsy punches (Kaimedical)
445 of 1 mm and 1.5 mm were used to cut individual photoacoustic films for *ex vivo* and *in vivo*
446 experiments.
447 To fabricate the 40-µm-thick PDMS-CNT film, we employed a recipe derived from previous work[10]. We
448 initially prepared PDMS at mix ratios of 10:1. Subsequently, a 15%wt of CNT (<8 nm OD, 2–5 nm ID,
449 length 0.5–2 µm, VWR, Inc., USA) was mixed with the PDMS, with the addition of IPA to facilitate CNT
450 dissolution. The resulting mixture underwent a 5-minute sonication process, followed by a 30-minute
451 degassing step to eliminate bubbles and IPA. The prepared mixture was then spin-coated onto a glass
452 substrate at 500 rpm for 5 minutes. The coated substrate was cured at 110 °C for 15 minutes.
453

454 ## Characterization of the photoacoustic properties of the films

455 The photoacoustic properties of the films were characterized with a 40-µm needle hydrophone system
456 (NH0040, Precision Acoustics Inc., UK) or an 85-µm needle hydrophone system (HGL-0085, Onda
457 Corporation, USA). Illumination was provided by a Q-switched diode-pumped laser with a pulse width
458 of 8 ns (RPMC, wavelength 1030 nm, repetition frequency 2.9 kHz, USA), delivered to one side of the
459 film via a multimode fiber with a 200-µm core (FT200UMT, Thorlabs, USA). On the other side of the
460 film, the hydrophone was mounted on a 3D stage and aligned with the area illuminated by the optical
461 fiber. The signals were amplified with a pulser-receiver (Olympus, Model 5073PR, USA) and then
462 recorded via a digital oscilloscope (Rigol, DS4024, USA).
463

464 **Mapping the photoacoustic pressure field**

465 Photoacoustic field microscopy was used to map the generated ultrasound field, as previously
466 reported[35]. Here a 1064-nm pulsed laser (OPOLETTE 355 LD, OPOTEK, pulse duration 5 ns) was used
467 as the pump beam. A continuous wave 1310-nm laser (1310LD-4-0-0, AeroDIODE Corporation) served
468 as the probe. A piece of PDMS/CS/PDMS film was mounted on a 50-µm optical fiber (FG050UGA,
469 Thorlabs), and the 1064-nm laser was delivered to the film sample to generate the photoacoustic
470 signals. A translation stage (ProScan III, Prior) was used to scan the generated ultrasound field. Under
471 a single ns pulse, the PA-induced refractive index change was detected as the imaging contrast.
472

473 **Temperature measurements**

474 A J-type thermocouple with a 200-µm tip was set against the PDMS/CS/PDMS film inside 3% agarose
475 gel, typically used for mimicking tissue[36]. The PDMS/CS/PDMS film was attached to a 200-µm optical
476 fiber to assure the alignment between the illuminated area on the film and the thermocouple tip. A
477 Q-switched diode-pumped laser with a pulse width of 4.5 ns (RPMC, wavelength 1030 nm, USA) was
478 used to illuminate the film. The temperature on the film was recorded with a 2 kHz sampling rate from
479 10 recordings. Average data was computed from the 3 recordings that showed the highest
480 temperature rise. Photos of the setup are shown in Supplementary Fig. S5. No transient temperature
481 events faster than the 2 kHz acquisition frequency are expected to occur (Supplementary Fig. S6).
482

483 **Animals**

484 All animal experiments were conducted at the Paris Vision Institute, in accordance with the National
485 Institutes of Health Guide for the Care and Use of Laboratory animals. Protocols were approved by
486 the Local Animal Ethics Committee (Committee Charles Darwin CEEACD/N°5, project reference
487 Apafis#40263-2023010909277429 v5) and conducted in agreement with Directive 2010/63/EU of the
488 European Parliament. Wild-type Long-Evans male rats aged between 2 and 8 months were obtained

489 from Janvier Laboratories. P23H male and female transgenic rats (9-14 months old) were raised locally.
490 P23H rats serve as a model for autosomal dominant retinitis pigmentosa[37].
491

492 ## *Ex vivo* experiments

493 ### *Ex vivo* retina preparation and blockers

494 The following procedures were carried out under dim red light. Animals were dark adapted for 30
495 minutes, then anesthetized with $CO_2$ and euthanized by cervical dislocation. The eyes were enucleated
496 and hemisected in carboxygenated (95% $O_2$, 5% $CO_2$) Ringer medium containing (in mM): 125 NaCl,
497 2.5 KCl, 1 $MgCl_2$, 1.25 $NaH_2PO_4$, 20 glucose, 26 $NaHCO_3$, 1 $CaCl_2$ and 0.5 L-Glutamine at pH 7.4. The
498 medium was continuously perfused in the recording chamber at a speed of 1.5 $mL.min^{-1}$ and was kept
499 around 37 °C.
500 Isolated retinae were placed on a dialysis membrane (Spectra/Por® 6 50 kD dialysis membrane,
501 Spectrum) coated with poly-L-lysine (0.1%, Sigma), with the photoacoustic film between the dialysis
502 membrane and the retina, and with photoreceptors against the film. The retinae were pressed against
503 a multi-electrode array (MEA) (MEA256 iR-ITO; Multi-Channel Systems, Reutlingen, Germany) with a
504 custom 3D-printed piece.
505 AMPA/kainate glutamate receptor antagonist 6-cyano-7-nitroquinoxaline-2,3-dione (CNQX, 20 µM,
506 Tocris Bioscience) and NMDA glutamate receptor antagonist (RS)-3-(2-carboxypiperazin-4-yl)-propyl-
507 1-phosphonic acid ((RS)-CPP, 10 µM, Tocris Bioscience) were bath-applied through the perfusion line.
508

509 ### *Ex vivo* photoacoustic retinal stimulation

510 Photoacoustic stimulations were done with a 1030-nm, 4.2-ns-pulsed laser (One DPSS, Bright
511 Solutions) delivered through a 200-µm-core 0.22 NA multimode SMA/SMA optic fiber (Thorlabs Inc,
512 USA., ref M25L01). A second 200-µm-core was connected to the first fiber using a fixed attenuator
513 (Thorlabs Inc., USA, ref FA26M) to control the power density. The optical fiber was inserted into a
514 custom 3D-printed holder incorporated in a motorized XYZ stage with 0.5-nm precision (Sensapex,
515 uMp-3 micromanipulator). It was lowered above the PA film at a ~90° angle and placed at a fixed (~ 1
516 mm) distance above the PA film. The illumination spot was measured ~300 µm in diameter on the film
517 using ImagJ and the MEA electrode pitch as reference. A low power 650-nm guiding beam
518 (FIBERCHECK, Laser Components) was used to calibrate the beam position relative to the MEA.
519 Laser pulse repetition rate and the laser burst trains were controlled using a Teensy microcontroller
520 custom written software (C++, Java, Python). In a typical stimulation, the laser delivered 10 µJ pulses
521 with a repetition frequency $f_{rep}$ of 1.9 kHz or 3.5 kHz during a single 5-ms to 30-ms burst, repeated at

522 1 Hz for 40 bursts. PA film integrity was confirmed by the lack of photoelectric effect in the MEA
523 recordings (Supplementary Fig. S7).
524
525 **Analysis of MEA recordings**
526 MEA raw traces were recorded through the MEA software (MC Rack, Multichannel Systems). Spikes
527 were sorted using SpyKING CIRCUS[38], manually curated using phy[39], and attributed to individual cells.
528 Spikes were referenced relative to stimulus onset and grouped across trials in bins using a sliding
529 window (bin width = 20 ms, increments = 5 ms). Cell activity in each bin was estimated using bootstrap
530 resampling (n = 1000 resamples, 99% confidence intervals), and considered significantly increased or
531 decreased if there were no overlapping confidence intervals compared to baseline (200 - 100 ms
532 before stimulus onset).
533 RGCs were considered responsive or modulated if their firing rate was significantly increased or
534 decreased compared to baseline for at least 15 ms consecutively, and response latency was defined
535 as the first bin of this series. Noise clusters were filtered from the cell clusters by excluding cells with
536 response latencies below 5 ms. A 300-µm-diameter area was illuminated by the 1030-nm laser (200-
537 µm fiber) during photoacoustic stimulation. For quantifying responsive cells and dose responses (Fig.
538 2 and 3), we included only cells within 300-µm of the center of the illuminated area ("stimulation
539 site"). The number of recorded cells per stimulation site is shown in Supplementary Fig. S8. Cells with
540 a response latency above 250 ms were excluded, as they were likely not a result from direct
541 stimulation.
542 To analyze the relation between cell modulation and distance from the stimulation area (Fig. 4a), we
543 calculated local averages in firing rate by assigning the firing rate of each cluster to a bin in a grid with
544 a spacing of 25 µm, and smoothing the resulting averages using a convolution with a gaussian kernel
545 (sigma = 100 µm).
546
547 ***In vivo* experiments**
548 Successful implantation was defined as good positioning of the 1-mm-diameter film in the subretinal
549 space, with no complications due to surgery. N = 8 adult (9-10 mo) P23H rats were successfully
550 implanted and used for biocompatibility studies. N = 7 adult Long-Evans rats were successfully
551 implanted at 8 weeks of age and used for photoacoustic stimulation.
552
553 **Surgery procedures for chronic subretinal implantation**
554 A 1-mm-diameter PA film was surgically placed in the subretinal space in the central region next to
555 the optic nerve, as previously described[40]. Briefly, a small sclerotomy was performed on the dorsal

556 sclera tangential to the cornea. A gel of sodium chondroitin sulfate-sodium hyaluronate (Viscoat
557 Alcon) was injected in the sclerotomy to generate a retinal detachment. The implant was then inserted
558 below the detached retina in the subretinal space, targeting a location adjacent to the optic disk.
559
560 **Ocular imaging**
561 Eye fundus imaging (MICRON® IV, Phoenix, USA) and optical coherence tomography (Bioptigen® OCT
562 system, Leica microsystems, Germany) were performed at 7 and 15 days post-implantation (dpi) for
563 all rats to monitor inflammation and confirm correct implantation. Additional imaging was conducted
564 at 30, 60, 90 and 120 dpi for rats that did not undergo prior retinal stimulation.
565
566 **Cranial window acute surgery**
567 Anesthesia was provided with an intraperitoneal injection of 40 $mg.kg^{-1}$ ketamine (Axience, France)
568 and 0.14 $mg.kg^{-1}$ medetomidine (Domitor®, Vétoquinol, France) diluted in sodium chloride. The animal
569 was placed on a stereotaxic frame to perform a left craniotomy. Drops of ocular gel (Lubrithal®,
570 Dechra, France) were applied and the eyes were then covered with a black cloth for dark adaptation.
571 A rectangular piece of bone was removed from Bregma -3 mm to -8 mm.
572
573 **Retinal stimulation and brain imaging**
574 Retinal stimulation was performed 26 - 40 days after implantation surgery for rats with
575 PDMS/CS/PDMS implants and 23 - 29 days after implantation surgery for PDMS-CNT implants, and
576 immediately after the cranial window surgery. Anesthesia was re-administered every 45 min with one-
577 third of the initial dose, up to a maximum of 5 injections. At the end of the experiment, the animals
578 were euthanized using an intracardiac injection (Exagon®, Axience, France).
579 For full field light stimulations with a white LED source, the light power on the retina was estimated
580 to be ~0.02 $mW.mm^{-2}$, based on the power entering the pupil of 1.2 mW. The choice of the stimulation
581 protocol was informed by prior retina studies using functional ultrasound imaging[40,41]. Each 1.8-s
582 stimulation sequence consisted of 6 evenly spaced 300-ms illuminations (LED on), repeated 15 times.
583 For 595-nm, 1030-nm laser stimulation and photoacoustic stimulation, focused laser spots were
584 aimed using a laser injector from the MICRON 810-nm Image-Guided Laser modality combined with a
585 MICRON® III camera (Phoenix, USA). A low power 650-nm guiding beam (FIBERCHECK, Laser
586 Components) was coupled to the injector to safely choose the area to stimulate. The rat's implanted
587 eye was covered in ocular gel (Lubrithal®, Dechra, France) and in contact with the camera lens.
588 Stimulation sequences for all 3 modalities were identical.

589 For 595-nm (continuous) laser stimulation, power density on retina was 26 µW in a 400 ± 26 -µm-
590 diameter laser spot. For photoacoustic stimulation, the same 1030-nm pulsed laser used in the *ex vivo*
591 experiments was employed. The laser energy exiting the laser injector was $E_p$ = 15 µJ per pulse. To aim
592 at the implant for photoacoustic stimulation, the laser focal spot was not placed on the optical axis of
593 the injector lens, which resulted in a loss of power. All the laser diameter at $1/e^2$ ($D_L$) and laser power
594 density P were estimated from average intensity profiles extracted with Fiji/ImageJ (Supplementary
595 Fig. S9 and S10) and are expressed as the mean ± standard deviation.
596
597 For 1030-nm laser stimulation on the retina: $D_L$ = 470 ± 70 µm. P = 0.56 ± 0.21 $W.mm^{-2}$,
598 for 1030-nm photoacoustic stimulation with PDMS-CNT implants: $D_L$ = 360 ± 60 µm. P = 0.39 ± 0.12
599 $W.mm^{-2}$,
600 for 1030-nm photoacoustic stimulation with PDMS/CS/PDMS implants: $D_L$ = 410 ± 45 µm. P = 0.29 ±
601 0.06 $W.mm^{-2}$.
602
603 The pupil of the eye of interest was dilated with a tropicamide-based eye drop solution (Mydriaticum®,
604 Théa, France) before the first recording. Body temperature was monitored with a rectal probe and
605 maintained using a heating blanket. Respiratory and heart rates were continuously monitored (TCMT,
606 Minerve, France). After local application of lidocaine (4 $mg.kg^{-1}$, Laocaïne®, MSD, France), the thinned
607 skull was exposed and covered with ultrasound gel. The rats were scanned with a system dedicated
608 to small animal ultrasound neuroimaging (Iconeus, Paris, France). Doppler vascular images were
609 obtained using the Ultrafast Compound Doppler Imaging technique[42]. The probe was positioned
610 coronally at Bregma - 6.5 mm in order to measure the cerebral blood volume (CBV) in the contralateral
611 superior colliculus. Each frame was a compound plane wave frame[43] resulting from the coherent
612 summation of backscattered echoes obtained after successive tilted plane waves emissions. Then, the
613 CBV signal was extracted from the tissue signal by filtering the image stacks with a dedicated
614 spatiotemporal filter using Singular Value Decomposition[44]. Each transcranial Power Doppler image
615 was obtained from 200 compounded frames acquired at 500 Hz frame rate.
616

617 ## Analysis of *in vivo* experiments

618 ### Analysis of OCT images

619 Mean retinal thickness next to and above the implant were measured with ImageJ on OCT images
620 (diametral slices). The number of rats imaged at 30 dpi and later was lower than the number imaged
621 at 7 dpi and 15 dpi because rats were used for terminal retinal stimulation recordings starting at 23
622 dpi.

**Analysis of functional ultrasound imaging recordings**

The correlation map of the CBV variations and the laser sequence for stimulation was computed by the manufacturer's proprietary IcoStudio software (v1.5.2). A delay of either 2 or 3 s was computed in the calculation of the correlation to account for vascular delay (the chosen value maximizes the correlation). In correlation map displays (Fig. 6c), only significant pixels with a correlation threshold greater than 0.2 are shown. Maps with a correlation threshold of 0.1 are shown in Supplementary Fig. S11. A 29-by-29-pixel (29 pixels = 302 ± 10 µm) region of interest (ROI) was defined for each animal, centered on the peak intensity of the correlation map for full-field-white-light stimulation. Relative CBV variations (rCBV) were extracted in this ROI for all stimulation types. For each recording (15 laser stimulations), the cerebral blood flow (CBV) was normalized into a relative steady-state value (rCBV) and calculated as the following: $rCBV = (CBV(t) - CBV_0)/CBV_0$, where CBV(t) is the power doppler value t seconds after the start of laser sequence, and $CBV_0$ is the baseline in the ROI. The baseline was defined as the mean power doppler value 5 seconds before the start of the laser sequence. The data was bootstrapped to calculate confidence intervals.

## Statistical analysis

Values are expressed as mean values ± standard error of the mean (SE) in figures and in the text, unless specified otherwise. Similarly, in scatter plots with error bars (Fig. 1, Fig. 3), data points and error bars represent the mean and the standard error of the mean, respectively.

Statistical significance was analyzed with Wilcoxon signed-rank tests and Mann-Whitney U tests (Fig. 2 to 6). Pearson correlation (Fig. 2 to 4) was computed to quantify the strength and direction of the linear relationship between two continuous variables. One-way ANOVA was used to test the effect of a single factor on the mean of a dependent variable (Fig. 5). Finally, to estimate confidence intervals for a statistic of unknown distribution (average rCBV variations in Fig. 6) we used bootstrapped estimation (1000 samples, 95% confidence intervals). Statistical tests are provided in the figure legends.

## Data availability

The data supporting the findings of this study are available from the corresponding author upon reasonable request.

### Code availability

The custom Python codes are available from the corresponding author upon reasonable request.

## Supplementary Information

Supplementary Information is available for this paper.


## Acknowledgements

This work was supported by the National Institute of Health, United States, through the BRAIN Initiative R01 NS109794 to J-XC and CY, BRAIN/NEI R21 EY035437 and NEI 1R21EY036579 to CY, by the Foundation Fighting Blindness (PPA-0922-0840-INSERM) to SP, by IHU FOReSIGHT, France, (ANR-18-IAHU-01) to SP, by the European Research Council (Grant Agreement 101045289) to SP, and by Axorus SAS, France, to SP and CY.


## Author Contributions

Equal contributions: A.L., Y.L. and TR.R, and S.P. and H.M.

A.L., Y.L., TR.R. and H.M. designed the experiments.

A.L., Y.L., TR.R., H.M., J.V., A.F., C-A.C., G.C., Y.Y., C.J., M.C. and J.D. carried out the experiments and analyzed the data.

J-D.L. and G.T. provided support for the experiments, study design and data analysis.

H.M., J-D.L., J-X.C., C.Y. and S.P. conceived the project, and contributed to study design and data interpretation.

A.L., Y.L., TR.R., C.Y.,H.M., and S.P. wrote the manuscript with input from all others.

## Competing interest declaration

This study was funded in part by the company Axorus SAS. J-DL and HM are major stakeholders in Axorus. CY and J-XC are minor stakeholders in Axorus.

## Materials & Correspondence

Correspondence and requests for materials should be addressed to:

serge.picaud@inserm.fr

helene.moulet@axorus.com

cheyang@bu.edu

jxcheng@bu.edu

688 ## References


689 1. Jeany Q Li *et al.* Prevalence and incidence of age-related macular degeneration in Europe: a
690 systematic review and meta-analysis. *Br. J. Ophthalmol.* **104**, 1077 (2020).
691 2. Da Cruz, L. *et al.* Five-Year Safety and Performance Results from the Argus II Retinal Prosthesis
692 System Clinical Trial. *Ophthalmology* **123**, 2248–2254 (2016).
693 3. Wu, K. Y., Mina, M., Sahyoun, J.-Y., Kalevar, A. & Tran, S. D. Retinal Prostheses: Engineering and
694 Clinical Perspectives for Vision Restoration. *Sensors* **23**, 5782 (2023).
695 4. Muqit, M. M. K. *et al.* Prosthetic Visual Acuity with the PRIMA Subretinal Microchip in Patients
696 with Atrophic Age-Related Macular Degeneration at 4 Years Follow-up. *Ophthalmol. Sci.* **4**,
697 (2024).
698 5. Lu, G. *et al.* Ultrasound Retinal Stimulation: A Mini-Review of Recent Developments. *IEEE Trans.*
699 *Ultrason. Ferroelectr. Freq. Control* **69**, 3224–3231 (2022).
700 6. Menz, M. D., Oralkan, Ö., Khuri-Yakub, P. T. & Baccus, S. A. Precise Neural Stimulation in the
701 Retina Using Focused Ultrasound. *J. Neurosci.* **33**, 4550–4560 (2013).
702 7. Gong, C. *et al.* Non-Invasive Hybrid Ultrasound Stimulation of Visual Cortex In Vivo.
703 *Bioengineering* **10**, 577 (2023).
704 8. Qian, X. *et al.* Noninvasive Ultrasound Retinal Stimulation for Vision Restoration at High
705 Spatiotemporal Resolution. *BME Front.* **2022**, 9829316 (2022).
706 9. Lu, G. *et al.* Noninvasive imaging-guided ultrasonic neurostimulation with arbitrary 2D patterns
707 and its application for high-quality vision restoration. *Nat. Commun.* **15**, 4481 (2024).
708 10. Shi, L. *et al.* Non-genetic photoacoustic stimulation of single neurons by a tapered fiber
709 optoacoustic emitter. *Light Sci. Appl.* **10**, 143 (2021).
710 11. Du, Z. *et al.* Photoacoustic: A Versatile Nongenetic Method for High-Precision Neuromodulation.
711 *Acc. Chem. Res.* **57**, 1595–1607 (2024).
712 12. Jiang, Q. *et al.* Temporal Neuromodulation of Retinal Ganglion Cells by Low-Frequency Focused
713 Ultrasound Stimulation. *IEEE Trans. Neural Syst. Rehabil. Eng.* **26**, 969–976 (2018).
714 13. Lee, H. C. *et al.* Histological evaluation of flexible neural implants; flexibility limit for reducing the
715 tissue response? *J. Neural Eng.* **14**, 036026 (2017).
716 14. Andersen, M. A. & Schouenborg, J. Polydimethylsiloxane as a more biocompatible alternative to
717 glass in optogenetics. *Sci. Rep.* **13**, 16090 (2023).
718 15. Menz, M. D. *et al.* Radiation Force as a Physical Mechanism for Ultrasonic Neurostimulation of
719 the *Ex Vivo* Retina. *J. Neurosci.* **39**, 6251–6264 (2019).
720 16. Zhuo, S.-Y. *et al.* Mechanism of low-frequency, low-intensity ultrasound modulation of the
721 mouse retina. *J. Neural Eng.* **20**, 036025 (2023).

722 17. Chen, G. *et al.* High-Precision Photoacoustic Neural Modulation Uses a Non-Thermal
723 Mechanism. *Adv. Sci.* **11**, 2403205 (2024).
724 18. Cadoni, S. *et al.* Ectopic expression of a mechanosensitive channel confers spatiotemporal
725 resolution to ultrasound stimulations of neurons for visual restoration. *Nat. Nanotechnol.* **18**,
726 667–676 (2023).
727 19. Naor, O., Hertzberg, Y., Zemel, E., Kimmel, E. & Shoham, S. Towards multifocal ultrasonic neural
728 stimulation II: design considerations for an acoustic retinal prosthesis. *J. Neural Eng.* **9**, 026006
729 (2012).
730 20. Palczewska, G. *et al.* Human infrared vision is triggered by two-photon chromophore
731 isomerization. *Proc. Natl. Acad. Sci.* **111**, (2014).
732 21. Vinberg, F. *et al.* Sensitivity of Mammalian Cone Photoreceptors to Infrared Light. *Neuroscience*
733 **416**, 100–108 (2019).
734 22. Rabell-Montiel, A., Anderson, T., Pye, S. D. & Moran, C. M. Attenuation Coefficients of the
735 Individual Components of the International Electrotechnical Commission Agar Tissue-Mimicking
736 Material. *Ultrasound Med. Biol.* **44**, 2371–2378 (2018).
737 23. Lorach, H. *et al.* Development of Animal Models of Local Retinal Degeneration. *Investig.*
738 *Opthalmology Vis. Sci.* **56**, 4644 (2015).
739 24. Prévot, P.-H. *et al.* Behavioural responses to a photovoltaic subretinal prosthesis implanted in
740 non-human primates. *Nat. Biomed. Eng.* **4**, 172–180 (2019).
741 25. FDA. Marketing Clearance of Diagnostic Ultrasound Systems and Transducers - Guidance for
742 Industry and Food and Drug Administration Staff. (2023).
743 26. Palanker, D., Vankov, A., Huie, P. & Baccus, S. Design of a high-resolution optoelectronic retinal
744 prosthesis. *J. Neural Eng.* **2**, S105 (2005).
745 27. Bhuckory, M. B. *et al.* Cellular migration into a subretinal honeycomb-shaped prosthesis for
746 high-resolution prosthetic vision. *Proc. Natl. Acad. Sci. U. S. A.* **120**, e2307380120.
747 28. Wang, B.-Y. *et al.* Electronic photoreceptors enable prosthetic visual acuity matching the natural
748 resolution in rats. *Nat. Commun.* **13**, 6627 (2022).
749 29. Van Den Berg, T. J. T. P. & Spekreijse, H. Near infrared light absorption in the human eye media.
750 *Vision Res.* **37**, 249–253 (1997).
751 30. Li, Y. *et al.* Optically-generated focused ultrasound for noninvasive brain stimulation with
752 ultrahigh precision. *Light Sci. Appl.* **11**, 321 (2022).
753 31. Du, X. *et al.* Lead halide perovskite for efficient optoacoustic conversion and application toward
754 high-resolution ultrasound imaging. *Nat. Commun.* **12**, 3348 (2021).
755 32. Noimark, S. *et al.* Polydimethylsiloxane Composites for Optical Ultrasound Generation and

Multimodality Imaging. *Adv. Funct. Mater.* **28**, 1704919 (2018).

33. Qiang, Z., Zhang, Y., Groff, J. A., Cavicchi, K. A. & Vogt, B. D. A generalized method for alignment of block copolymer films: solvent vapor annealing with soft shear. *Soft Matter* **10**, 6068–6076 (2014).
34. Duangkanya, K., Kopwitthaya, A., Chanhorm, S. & Infahsaeng, Y. Oxygen plasma treatment time induced hydrophilicity of polydimethylsiloxane (PDMS) thin films for liquid lenses application. *Mater. Today Proc.* **65**, 2442–2445 (2022).
35. Cheng, J.-X. *et al.* Millimeter-deep micron-resolution vibrational imaging by shortwave infrared photothermal microscopy. *Res. Sq.* rs.3.rs-3449548 (2023) doi:10.21203/rs.3.rs-3449548/v1.
36. Chen, P. *et al.* Acoustic characterization of tissue-mimicking materials for ultrasound perfusion imaging research. *Ultrasound Med. Biol.* **48**, 124–142 (2022).
37. Orhan, E. *et al.* Genotypic and Phenotypic Characterization of P23H Line 1 Rat Model. *PLOS ONE* **10**, e0127319 (2015).
38. Yger, P. *et al.* A spike sorting toolbox for up to thousands of electrodes validated with ground truth recordings in vitro and in vivo. *eLife* **7**, e34518.
39. Rossant, C. *et al.* Spike sorting for large, dense electrode arrays. *Nat. Neurosci.* **19**, 634–641 (2016).
40. Provansal, M. *et al.* Functional ultrasound imaging of the spreading activity following optogenetic stimulation of the rat visual cortex. *Sci. Rep.* **11**, 12603 (2021).
41. Morisset, C. *et al.* Retinal functional ultrasound imaging (rfUS) for assessing neurovascular alterations: a pilot study on a rat model of dementia. *Sci. Rep.* **12**, 19515 (2022).
42. Bercoff, J. *et al.* Ultrafast compound doppler imaging: providing full blood flow characterization. *IEEE Trans. Ultrason. Ferroelectr. Freq. Control* **58**, 134–147 (2011).
43. Montaldo, G., Tanter, M., Bercoff, J., Benech, N. & Fink, M. Coherent plane-wave compounding for very high frame rate ultrasonography and transient elastography. *IEEE Trans. Ultrason. Ferroelectr. Freq. Control* **56**, 489–506 (2009).
44. Demene, C. *et al.* Spatiotemporal Clutter Filtering of Ultrafast Ultrasound Data Highly Increases Doppler and fUltrasound Sensitivity. *IEEE Trans. Med. Imaging* **34**, 2271–2285 (2015).